Probing Bias-Dependent Electrochemical Gas–Solid Reactions in $(La_xSr_{1-x})CoO_{3-\delta}$ Cathode Materials

Amit Kumar, Francesco Ciucci, Donovan Leonard, Stephen Jesse, Mike Biegalski, Hans Christen, Eva Mutoro, Ethan Crumlin, Yang Shao-Horn, Albina Borisevich, and Sergei V. Kalinin**

Spatial variability of bias-dependent electrochemical processes on a $(La_{0.5}Sr_{0.5})_2CoO_{4\pm\delta}$ modified $(La_xSr_{1-x})CoO_{3-\delta}$ surface is studied using first-order reversal curve method in electrochemical strain microscopy (ESM). The oxygen reduction/evolution reaction (ORR/OER) is activated at voltages as low as 3–4 V with respect to bottom electrode. The degree of bias-induced transformation as quantified by ESM hysteresis loop area increases with applied bias. The variability of electrochemical activity is explored using correlation analysis and the ORR/OER is shown to be activated in grains at relatively low biases, but the final reaction rate is relatively small. At the same time, at grain boundaries, the onset of reaction process corresponds to larger voltages, but limiting reactivity is much higher. The reaction mechanism in ESM of mixed electronic-ionic conductor is further analyzed. These studies both establish the framework for probing bias-dependent electrochemical processes in solids and demonstrate rich spectrum of electrochemical transformations underpinning catalytic activity in cobaltites.

1. Introduction

Direct conversion of chemical to electrical energy in fuel cells opens pathway to high energy density, high efficiency, and scalable energy generation devices.[1–3] Among these, high temperature solid oxide fuel cells (SOFC) offer the highest energy conversion efficiency approaching the thermodynamic limits. Similarly, fuel cell devices combining an energy generation unit with (potentially unlimited) fuel storage enable high energy storage densities, resulting in interest to these energy sources from mainstream computer, medical, and housing industry and military applications.[4] Finally, a lack of moving parts in the energy conversion systems creates the opportunity for virtually unlimited scaling from 100 MV power plants units to microscale energy sources for mobile robots and portable electronics.[5–7]

Despite the unique potential of fuel-cell based technologies, broad implementation of these devices faces a number of challenges related to life times and costs. The key aspect of fuel cell operation is the oxygen reduction reaction (ORR), i.e., transfer of oxygen species from gas to solid phase with simultaneous release of electrons. Low-temperature fuel cells typically require expensive Pt-based catalysts, a major factor driving the operational costs.[1] In high-temperature SOFC, the use of transition metal oxide cathodes at high temperatures obviates these problems, but imposes stringent limitations on mechanical stability and life times. These considerations have resulted in extensive search towards intermediate and low temperature fuel cell cathode materials,[8–11] as well as exploration of the chemical[12,13] and structural factors[14] that control ORR activity at low temperatures. Recently, it has been shown that operation of many oxide cathode materials can be associated with significant changes of material microstructure, including crystallization-amorphization[15] and surface cation enrichment.[16,17] These processes, reminiscent of poisoning and activation of catalyst systems, allow significant degree of control of cathode activity and enable strategies for activity enhancement.[18]

Optimization of SOFC materials requires understanding of elementary operation mechanisms[19] and their link to local microstructure and device architecture, as well as evolution of materials microstructure during the operation and degradation. Previously, we reported local measurements of reversible ORR activity on bare and Pt-functionalized yttria-stabilized zirconia (YSZ)[20] and $(La_xSr_{1-x})CoO_{3-\delta}$ ($LSCO_{113}$) surfaces as a function of composition and surface modification[21] using the electrochemical strain

Dr. A. Kumar, Dr. S. V. Kalinin
The Center for Nanophase Materials Sciences
Oak Ridge National Laboratory
Oak Ridge, TN 37831, USA
E-mail: amkum1in@gmail.com; sergei2@ornl.gov
Prof. F. Ciucci
Department of Mechanical Engineering & Department of Chemical and Biomolecular Engineering
The Hong Kong University of Science and Technology
Clear Water Bay, Kowloon, Hong Kong
Dr. D. Leonard, Dr. S. Jesse, Dr. M. Biegalski, Dr. H. Christen, Dr. A. Borisevich
The Center for Nanophase Materials Sciences
Oak Ridge National Laboratory
Oak Ridge, TN 37831, USA
Dr. E. Mutoro, E. Crumlin, Prof. Y. Shao-Horn
Department of Mechanical Engineering
Massachusetts Institute of Technology
Cambridge, MA 02139, USA

DOI: 10.1002/adfm.201202401

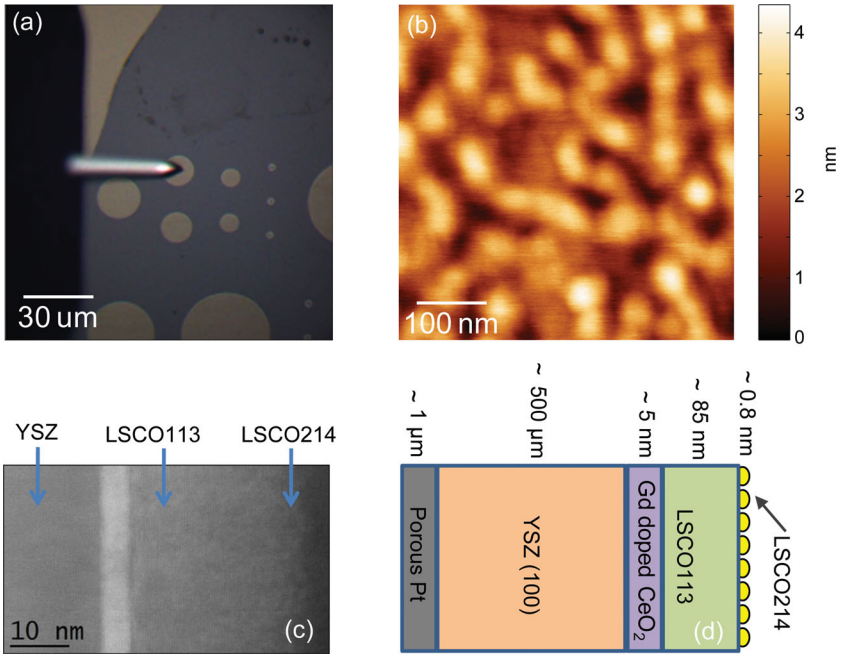

Figure 1. a) Optical microscopy image of patterned $LSCO_{214/113}$ microelectrodes, and b) topographic AFM image of the surface. c) High angle annular dark field STEM image of the film cross-section. Band of bright contrast corresponds to the 5 nm GDC buffer layer; d) Schematic of the patterned ~86 nm $LSCO_{214/113}$ microelectrodes, electrolyte and Pt counter electrode. The microfabricated electrodes are formed by $LSCO_{214/113}$ layer, with exposed GDC/YSZ surface in between.

microscopy (ESM) approach. Here, we develop experimental framework and explore bias evolution of local electrochemical processes in LSCO cathode using ESM and spatially resolved multidimensional voltage spectroscopies. The role of the grain boundaries on voltage-dependent mechanism of gas solid reaction is explored and the mechanism of ESM contrast formation is established.

2. ESM in Reversible Regime

As a model system, we have chosen the $(La_{0.5}Sr_{0.5})_2CoO_{4\pm\delta}$/$(La_{0.8}Sr_{0.2})CoO_{3-\delta}$ system, further referred to as $LSCO_{214/113}$, grown on the yttria-stabilized zirconia (YSZ) substrate with intermediate Gd-doped CeO_2 (GDC) buffer layer. The ORR functionality of these materials was extensively studied previously.[6,16,22] Here, we choose a system with ≈0.8-nm-thick $(La_{0.5}Sr_{0.5})_2CoO_{4\pm\delta}$ surface decoration of $LSCO_{113}$, which was shown to possess the highest ORR activity both in global[16] and local studies. The use of ionically conductive and electronically blocking GDC/YSZ electrolyte in conjunction with patterned electrodes allows minimizing electronic leakage currents, inevitable in mixed electronic-ionic conductors, that can lead to local heating or dielectric breakdown. For this material, the irreversible surface deformation under application of electric bias (a signature of irreversible bias-induced transformation) can be established, whereas for materials with lower ORR activity dielectric breakdown at higher voltages is typically observed. This allows ESM spectroscopic measurements to be performed systematically, i.e., application of voltage that exceeds local limit of surface stability is not associated with critical damage to surface or ESM tip.

The overall device architecture and structure is shown in **Figure 1**. The optical micrograph of the patterned LSCO/YSZ device surface during the ESM experiment is shown in Figure 1a, illustrating multiple $LSCO_{214/113}$ microelectrodes. The atomic force microscopy (AFM) and scanning transmission electron microscopy (STEM) images of the surface are shown in Figure 1b,c, with overall device schematic in Figure 1d. This topography is significantly different from that expected to LSC_{113} epitaxial perovskite films, and suggests possible changes in surface structure due to intermixing and phase evolution on the level of several unit cells. The STEM image clearly demarcates the YSZ, GDC layer, LSC_{113} film and LSC_{214} particles (seen between LSC_{113} and the dark carbon capping layer on the right). The microscopy data illustrates the presence of ≈1.5 nm scale surface roughness, comparable to thickness of the layered perovskites $(La_{0.5}Sr_{0.5})_2CoO_{4\pm\delta}$ layer and likely associated with the growth mode of 214 layer.

To explore the bias-induced reversible and hysteretic electrochemical processes in the device structures, we employ recently developed ESM method[23,24] and further extend it to multidimensional spectroscopic method to probe bias-dependent electrochemical mechnisms, as discussed below. In ESM, the scanning probe microscopy tip is used to apply electric bias to materials surface locally, effectively acting as mobile nanoelectrode. The applied bias induces ionic motion and local reversible and irreversible electrochemical processes.[25] Depending on the nature of material and bias applied, we classify the observed behaviors as: 1) reversible, where no hysteresis is observed, thus corresponding to the case of absent or very rapid tip-induced processes; 2) hysteretic, if hysteresis loops are observed, corresponding to the case of slow reaction or multiple remanent states which can all be achieved during bipolar bias sweep (i.e., response to periodic bias is cyclostationary); or 3) irreversible, when surface deformations are observed or hysteresis loops are not stationary, and system cannot be returned to initial state by any bias sequence.

The localization of electrochemical process is determined by the relative ionic and electronic transport properties of the system. For materials with purely ionic conductivity, the electric field and resultant concentration field are localized below the tip,[20,25] giving rise to high locality of the reaction region. For mixed ionic-electronic conductors (MIEC), the localization of the electrochemical process can be significantly more complicated and will be controlled by the electric field distribution in the device structure and ionic generation in the tip-surface junction, as explored in the present work. The change in molar volume of material due to ionic redistribution or phase transformations is detected through local surface displacement as

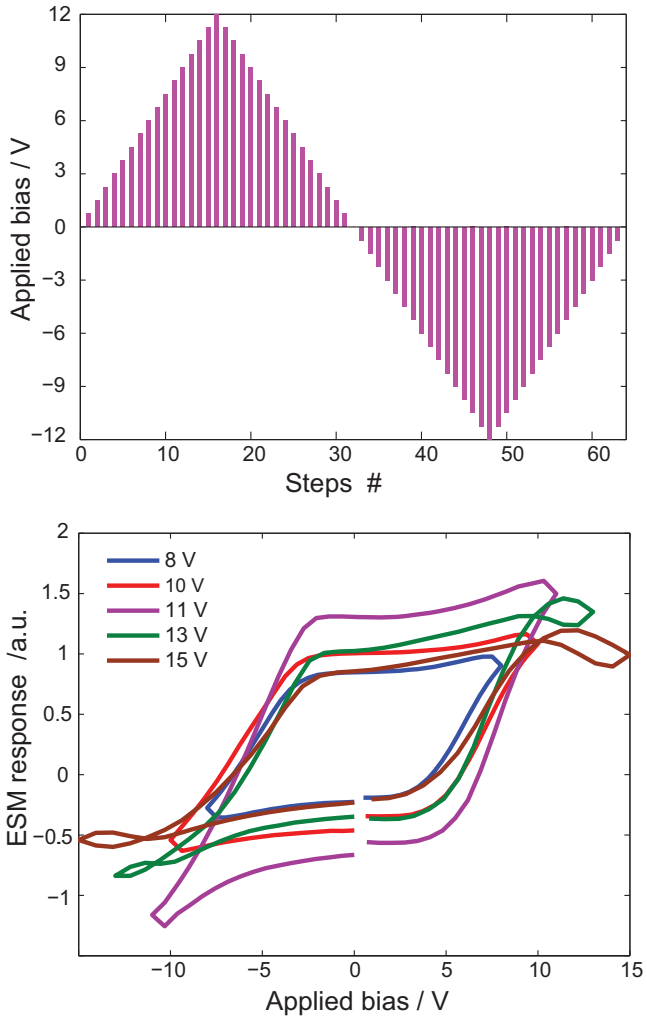

Figure 2. a) Bias envelope of the dc voltage applied during a ESM hysteresis loop measurement with the bias window of 12 V. b) ESM hysteresis loops on $LSCO_{214/113}$ thin film for different bias windows. The loops were averaged over 900 locations over 1 μm^2 area each.

measured by the ESM tip (electrochemical strain detection).[26] The theory of the tip-induced ESM in reversible and hysteretic regimes for diffusion-coupled systems has been discussed in detail,[25] as well as several simplified cases for mixed ionic-electronic conductors.[27,29]

While the electrochemical process and ionic motion can be localized to tip-surface junction, or occur everywhere on materials surface (e.g., for the case of high electronic conductivity of MIEC), the strain detection is always local as defined by SPM geometry. While the detailed theory for mechanisms of ESM is still under development, the corresponding limiting cases are offered by the piezoresponse force microscopy (PFM) of the ferroelectric materials. For local reaction process (e.g., for purely ionic material) the resolution and signal generation volume are limited by tip-surface contact radius, similar to tip-electrode geometry of PFM.[30] For MIECs with bulk electrochemical reaction, the system is analogous to ferroelectric capacitors and, for thin films, resolution is expected to be controlled by materials thickness.[31] For MIECs with uniform surface reaction, the resolution will be determined by the corresponding frequency-dependent transport length, as briefly analyzed elsewhere.[21] Practically, the resolution of ESM provides a measure of detected volume (similar to PFM[32]) if direct and indirect topographic cross-talk[33] can be excluded.

Here, we probe the electrochemical activity on the $LSCO_{214/113}$ surface using ESM voltage spectroscopy, as illustrated in **Figure 2**. In this, the ESM response is measured after the application bias pulse of predefined amplitude, with the pulse envelope following a triangular waveform, as shown in Figure 2a. The maximal amplitude of triangular wave is referred to as bias window. To increase signal to noise ratio through resonance enhancement of surface vibrations while avoiding the indirect topographic cross-talk, the measurements are performed using band-excitation method.[34,35] The details of data acquisition and processing for ferroelectric[36,37] and electrochemical[38] systems are discussed in a number of recent publications and are not repeated here.

The evolution of ESM hysteresis loops with bias window on the $LSCO_{214/113}$ surface are shown in Figure 2b. At low biases, the hysteresis loop is closed (not shown), while it opens up and saturates for higher biases. This behavior can be interpreted as following.[20,39] For low biases corresponding to reversible regime, field-induced vacancy and electronic motion are possible but the total amount of vacancies is preserved. Above critical bias for activation of electrochemical process, the vacancy injection in materials becomes possible; the hysteresis loop opens up and adopts classical shape with well-defined nucleation biases. The critical potential for this process are determined both by local electrode polarization (i.e., difference between thermodynamic redox potential and local potential driving the ORR/OER process) and electrochemical potential drop in the material (electrochemical voltage divider), and hence are larger than thermodynamic potentials for uniform fields. Note that in this hysteretic regime for ESM, the electrochemical process can be repeated for many cycles with minimal irreversible (by bias) changes in system state.

In the spectroscopic mapping ESM, the hysteresis loops similar to that in Figure 2 are acquired at each spatial location on 60×60 grid, yielding 3D data set. The effective parameters (e.g., area under the loop and nucleation biases) are then plotted as 2D maps, providing information on the spatial variability of electrochemical behavior. The fitted loop parameters show remarkable contrast in terms of loop height (**Figure 3**e) and loop area (Figure 3f). For uniform Vegard coefficients, these parameters are related to the diffusivity of ionic transport in the material (i.e., amount of ionic species injected due to the reaction in the tip-surface junction during the bias sweep). On the other hand, the nucleation biases show relatively weak contrast, thereby suggesting that relative variability of biases required to activate the ORR/OER process in the material surface is weak (or, equivalently, higher noise level in these parameters precludes correlations with the structure to be established). The histograms for positive bias distribution (PNB) and negative bias distribution (NNB) are diffused and the separation between the peaks is small, of the order of ≈1 V, suggesting that ORR/OER activity is readily induced in the material. (Figure S2, Supporting Information).

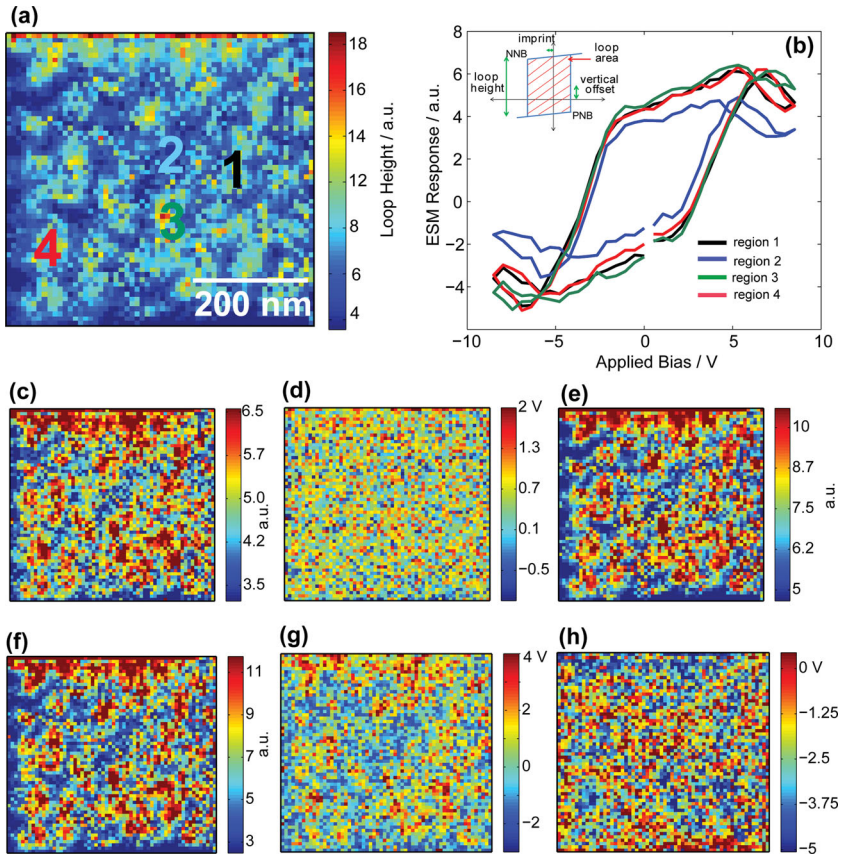

Figure 3. a) Loop height on 0.5 μm^2 area of $LSCO_{214/113}$ thin film. The averaged loops collected for a maximum bias of 8 V from selected regions on the map are shown in (b). The spatial variation of fitted loop parameters including c) vertical loop offset, d) imprint, e) height (with a compressed scale for visual clarity), f) area, g) positive nucleation bias (PNB), and h) negative nucleation bias (NNB).

3. FORC ESM Measurements

The limitation of the ESM spectroscopic mapping approach, as illustrated in Figure 2b, is that the hysteresis loop shape is strongly dependent on excitation window. While for materials with known loop formation mechanism (e.g., tip induced polarization switching) the limitations of this approach are well-understood and quantitative information can be extracted, e.g., for well saturated loops.[40,41] However, this is not the case for ESM with possible multiple voltage dependent electrochemical strain generation mechanisms (e.g., transport of several ionic species or several electrochemical reactions activated at different tip biases). Note that this uncertainty is universal for hysteretic systems, where knowledge of system response for a specified field history is insufficient to predict it for alternative histories.[42]

To avoid the uncertainty with the choice of the bias window in ESM spectroscopy and get insight into full spectrum of strain-coupled electrochemical processes induced by the ESM probe, here we use the first order reversal curve (FORC) method. In this, the envelope of probe bias is a bipolar excitation waveform with increasing amplitude. This allows multiple hysteresis loops with increasing bias window to be collected sequentially at each spatial location, providing the advantage of perfect spatial synchronization.

The data acquisition in FORC ESM spectroscopy is illustrated in **Figure 4**. Figure 4a illustrates the outer envelope of modulation waveform comprising multiple hysteresis loops. Note that detection is performed in the off-states following the application of bias pulse, similar to Figure 2a. The corresponding responses at single location are shown in Figure 4b,c, illustrating signal evolution as a function of bias and frequency. Note that these spectrograms are acquired at each point of the surface for spatially resolved measurements, giving rise to 5D data sets (response vs. location in 2D spatial grid, frequency, bias window, and bias). From the frequency deconvolution of these data, the electromechanical response signal is determined as shown in Figure 4d.

The evolution of the response with bias window provides information on sequential activation of electrochemical processes below the ESM probe. For low biases the response is bias independent (no reaction) while for larger bias windows than ≈5 V the hysteretic behavior is observed, where the jump at ≈100 voltage steps (corresponding to ≈5 V, Figure 4d) depicts the onset of gas-solid electrochemical reactivity. On further bias increase, the area under the hysteresis loop increases and then saturates, as discussed below.

The FORC ESM data can be represented as a series of hysteresis loops (FORC set) as shown in Figure 4e. The loops show universally comparable nucleation biases, suggesting similarity of underpinning electrochemical processes. The influence of bias on the hysteresis loop area is shown in Figure 4f, having transitions from closed hysteresis loops at low biases to gradual loop opening to saturation at high biases. The saturation can be attributed to the regime when the transport length of mobile ionic species becomes larger than the characteristic detection volume of SPM as determined by tip-surface contact radius (i.e., strains generated at large distances from contact do not transfer effectively to the tip).

The FORC ESM measurements can be performed on a dense spatial grid, providing information on spatial variability of hysteretic behavior. The influence of bias window on the area under hysteresis loops is shown in **Figure 5**. For low biases below 4.5 V, the loops are closed everywhere on the surface whereas for higher biases the loops open up. The ideal spatial correlation between the sequential images allows exploring the evolution of hysteresis loop parameters with bias, hence inferring their relationship to microstructure. It is interesting to note that the characteristic grain-like structure observed at biases greater than 4.5 V, with low response in the grain centers and enhanced response at the grain boundaries.

Figure 5a shows progressive activation of the surface electrochemical reactivity with tip bias measured with perfect spatial

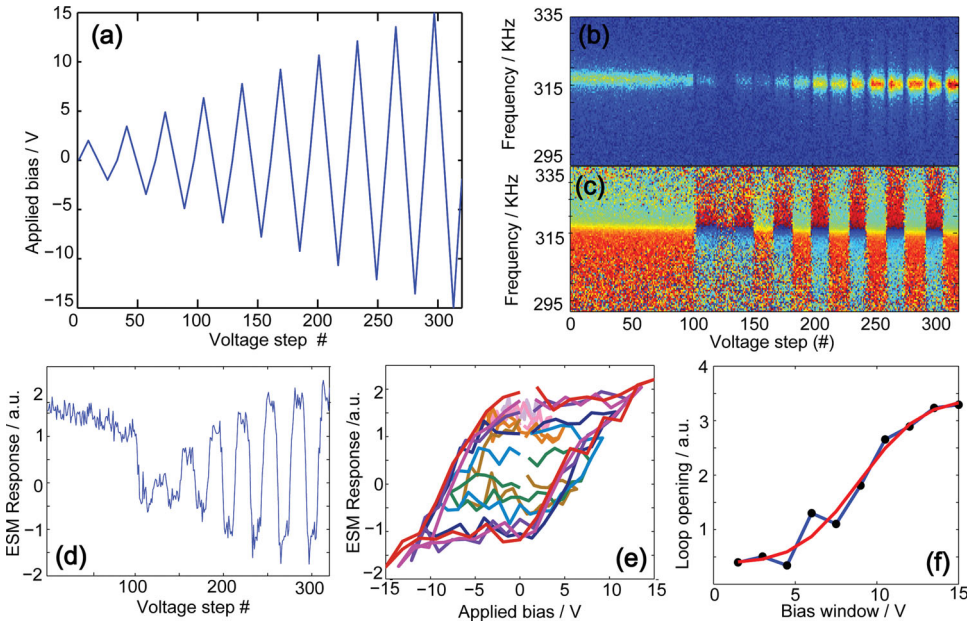

Figure 4. a) Bias scheme for obtaining first order reversal curves with increasing bias window on $LSCO_{214/113}$ thin film, b) amplitude spectrogram and c) phase spectrogram obtained at a single pixel. d) ESM response with increasing voltage step, e) first-order reversal curve hysteresis loops series, and d) loop opening vs. bias window fitted using an empirical model Equation 1.

alignment. However, large number of features precludes qualitative examination of the data. Parenthetically, imaging with high grid point densities and smaller scan sizes lead to rapid accumulation of surface damage and tip degradation. To circumvent this problem and explore this behavior systematically, we have calculated cross-correlation matrix defined for two matrices A and B of equal size as:

$$r = \frac{\sum_m \sum_n (A_{mn} - \overline{A})(B_{mn} - \overline{B})}{\sqrt{(\sum_m \sum_n (A_{mn} - \overline{A})^2)(\sum_m \sum_n (B_{mn} - \overline{B})^2)}} \quad (1)$$

where $\overline{A}$ = mean(A) and $\overline{B}$ = mean(B).

The cross-correlation between two images acquired at different biases (or times) establish the measure of resemblance between the two, with correlation coefficient of 1 meaning that features in both images are identical, -1 being opposite (minimum in one corresponds to maximum in the other), and 0 meaning that the images are unrelated. The single profile for cross-correlation with one of the largest bias window is shown in Figure 5b, whereas full cross-correlation matrix is shown in Figure 5c. While for large voltages (>10 V) cross-correlation values are close to 1 (i.e., images are similar), the cross-correlation between images acquired in the range from 3.5 to 7 V is negative. This observation suggests that electrochemical activity is first activated as select locations (e.g., grains), but for higher biases the activity is concentrated at different locations (e.g., grain boundaries, as can be deduced from image analysis).

To gain further insights in the spatial variability of response, we note that, in most locations, the loop opening shows characteristic sigmoidal shape. The universality of this behavior can be illustrated by principal component analysis of the data (not shown), suggesting significant spatial variability only in the first two principal component maps. This suggests that given experimental noise limitations, the spatial variability of hysteresis responses can be described by function with small number of independent parameters. In the absence of a priori physical models for FORC loop behavior, we describe hysteresis loop opening using a phenomenological model defined by

$$Y = a\,\mathrm{erf}\left(\frac{x-b}{s}\right) + c \quad (2)$$

where Y is hysteresis loop opening (area under the loop for each bias cycle), x is bias window, a is amplitude, b is critical voltage, c is initial offset and s is width of transition. The loop opening was calculated across the bias scheme at each pixel and was fitted across the 10 bias loops to the above defined model. The fit parameters are shown in **Figure 6**c–f and illustrate highly non-uniform grain-like activity pattern.

To quantify this behavior further, for each parameter map we have selected regions in the bottom 20% percentile of parameter value, top 20%, and intermediate, and plotted the hysteresis loop opening vs. bias averaged over these groups. The resultant behavior is shown in Figure 6g–i. Note the qualitative agreement of observed behavior with the cross-correlation analysis: in some regions the reaction onset corresponds to lower voltages, but the process rapidly saturates and the signal starts to decrease. At the same time, at other locations the reaction onset corresponds to larger biases, but the reaction develops to a larger extent. The rate of hysteresis loop opening (maximum derivative) with bias is comparable with all regions.

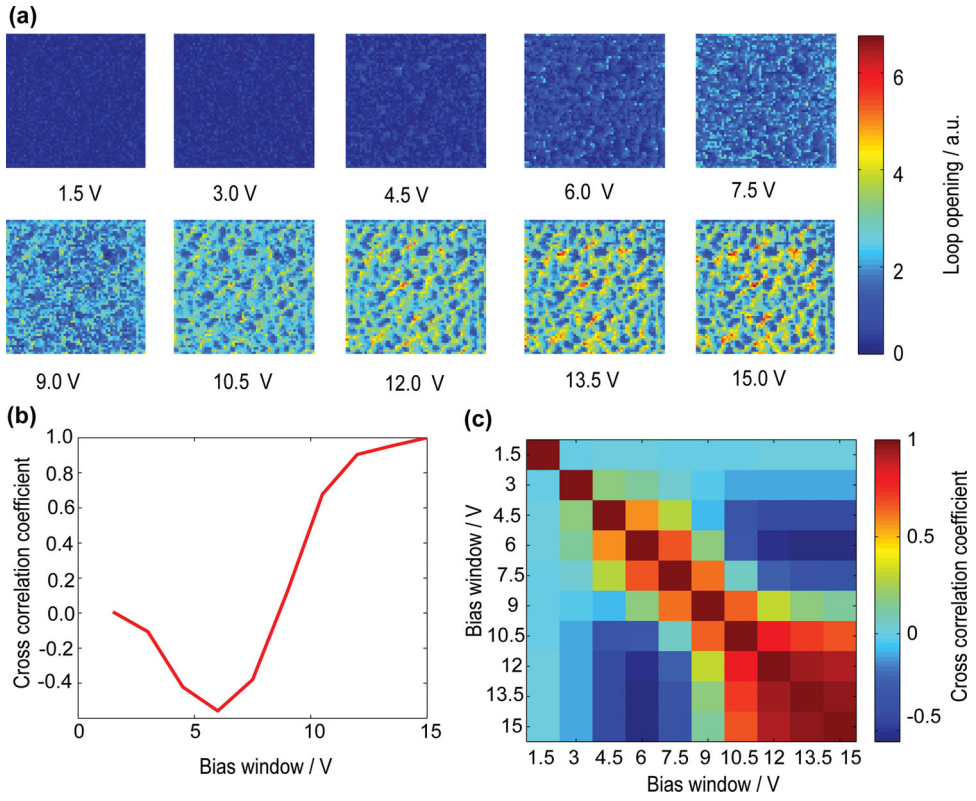

Figure 5. a) Loop opening during FORC measurements on 0.8 nm $LSCO_{214/113}$ thin film plotted for increasing bias windows. b) The cross correlation coefficient for the 15 V images with other images reveals mechanistic change in the loop opening process c) cross correlation matrix for the 10 different images shown in (a).

Comparison with the ESM activity maps suggests that the reaction is first initiated at grains, whereas grain boundary regions correspond to higher activity for large biases. Hence, this analysis allows voltage dependence of reaction rates at different microstructural elements to be differentiated.

4. The Local and Non-Local ESM on LSCO Structures

Finally, we discuss the localization of electrochemical reaction in the ESM of MIEC. Note that the reaction process is determined both by the accessibility of the gas phase (classical concentration limitation) and local overpotential due to the tip bias. The accessibility of the gas phase is maximal away from the tip, decreases towards the tip-surface contact, and can be expected to be zero in the tip-surface contact area. At the same time, the tip induced potential is maximal directly below and adjacent to the tip-surface contact, suggesting potentially non-trivial reaction localization and signal generation volumes. Note that this limitation, further referred to as shadowing effect, is specific to ESM and will not be expected for current-detection methods (e.g., for the limiting case of large metallic electrode on top of MIEC, measured current will correspond to that due to ORR/OER on free MIEC surface, whereas the strain below metal electrode will be zero).

Notably, the LSCO possess high electronic conductivity, suggesting that bias is applied uniformly across the surface. In this case, the processes in the tip-surface system can be described as shown in **Figure 7**. Application on bias to the cap through the tip induces oxygen evolution reaction (OER) $2O_O^x - 4e^- \rightarrow 2\,V_x^{\bullet\bullet} + O_2$ for positive biases and ORR process, $2\,V_x^{\bullet\bullet} + O_2 + 4e^- \rightarrow 2O_O^x$, for negative biases over the whole $LSC_{214//113}$ surface. The electrons are provided though the SPM tip. The electronic flow through tip-surface junction is balanced by vacancy flow through LSCO-YSZ interface. The strain generation is then global, whereas detection is local, somewhat similar to piezoresponse force microscopy of capacitor structures. This assumption agrees with difficulty in ESM imaging on un-patterned LSCO films, for which the effective resistance of cap-electrolyte region is lower and hence balancing electronic current in tip-surface junction is higher, and breakdown (controlled by total current) occurs easier.

The assumption that ORR/OER can even at low temperatures under strong bias stresses is well-established in literature. For SOFC-relevant materials, J. Fleig et al. observed ORR on YSZ at 400 °C and below.[43] Similarly, electroresistive materials and devices based on TiO_2, $SrTiO_3$, NiO, etc. that have attracted much attention in recent years[44–48] are based on room-temperature electrochemical processes in oxides. The tendency for oxygen bubble formation on surfaces and interfaces in memristors further verify this concept.[49] Finally, to complement solid-gas reaction, vacancy transport in oxides in strong fields was recently demonstrated for a variety of perovskites such as $SrTiO_3$ and $BiFeO_3$.[50–52] These considerations

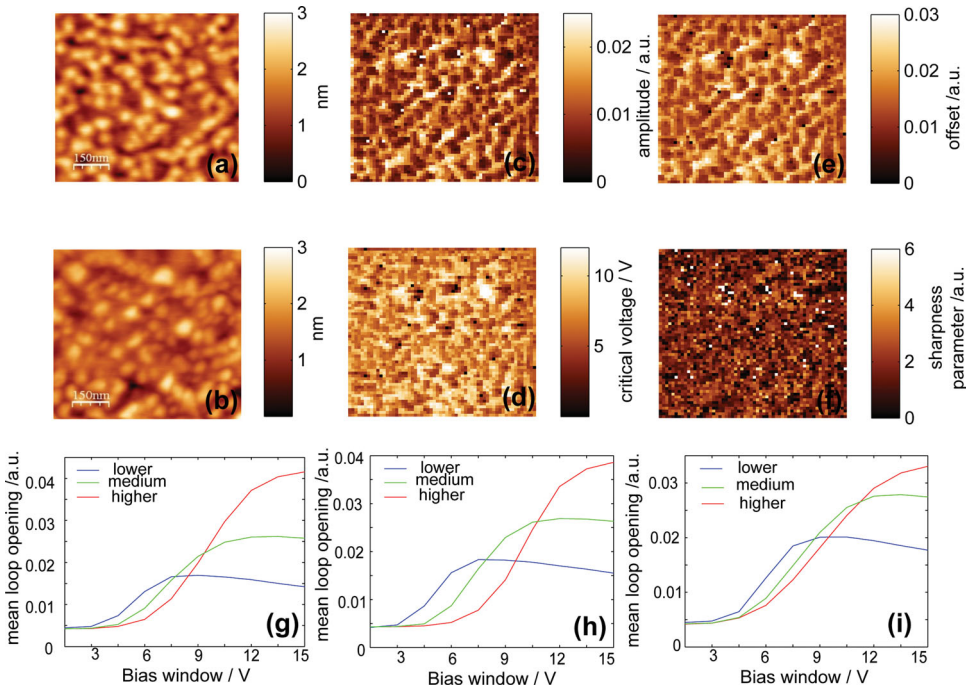

Figure 6. Topography on $LSCO_{214/113}$ thin film a) before and b) after FORC ESM measurements. Parameter maps of c) amplitude, d) critical voltage, e) offset, and f) transition sharpness parameter obtained after fitting the spatial data with a modified error function g) mean loop opening curves obtained from pixels with lower amplitude (less than 20% of all pixels), medium amplitude (more than 20% and less than 80% of all pixels) and high amplitude (more than 80% of all pixels) h) mean loop opening curves for critical voltage i) mean loop opening curves for transition sharpness parameter.

suggest that ORR/OER process and ionic transport are feasible over the present lengthscale at the experimental conditions, and hence observed responses can indeed correspond to ORR/OER processes (possibly assisted by catalytic water effects, etc). Note that irreversible reactions are also possible, but were not detected in the present set-up (i.e., no static deformation of surface was observed after measurements).

4.1. Numerical Modelling of Tip-Surface Contact

Finally, to estimate the geometry of the reaction zone (i.e., shadowing effect) and tip-surface currents in an ESM experiment, we perform finite element modeling of the ORR/OER process in the ESM geometry adapting an approach developed by Ciucci et al.[53] based on direct solution of Nernst-Planck equations under the electroneutrality condition. This consists in solving the following equation for the conducting species:

$$\frac{\partial c_k}{\partial t} + \nabla \cdot \left(-\frac{D_k c_k}{k_B T} \nabla \tilde{\mu}_k \right) = 0 \tag{3}$$

Where c_k is the concentration of species k, $\tilde{\mu}_k$ is the electrochemical potential of k, D_k is the diffusivity of k. The electrochemical potential is the sum of the chemical potential and the electrical potential energy of species k, $\tilde{\mu}_k = \mu_k + z_k e\phi$, where z_k is the integer charge of k and ϕ is the electrical potential.

Since $La_{1-x}Sr_xCoO_{3-\delta}$ is metallic and the electron conductivity is many orders of magnitude higher than the ionic conductivity, we take that the electrochemical potential of electrons $\tilde{\mu}_{eon}$ is uniform within the device. The chemical potential for the electrons is given by the rigid band model as developed by Lankhorst[54,55]

$$\mu_{\text{eon}} = \mu^0_{\text{eon}} + \frac{n - n^0}{g(\varepsilon_F)} \tag{4}$$

where $g(\varepsilon_F)$ is the density of states at the Fermi energy. The ionic chemical potential is instead given by[56]

$$\mu_{\text{ion}} = \mu^0_{\text{ion}} + k_B T \log\left(\frac{\delta}{3-\delta}\right) \tag{5}$$

Regarding the boundary conditions for Equation 3, the LSCO|GDC interface is set to be at equilibrium, i.e., the ionic transfer at that interface is assumed to be fast with respect to other transport processes. The

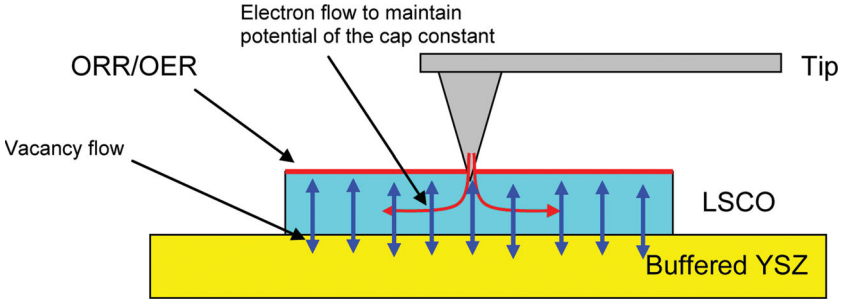

Figure 7. Ionic and electronic current distributions in the ESM of mixed-electronic-ionic conductors.

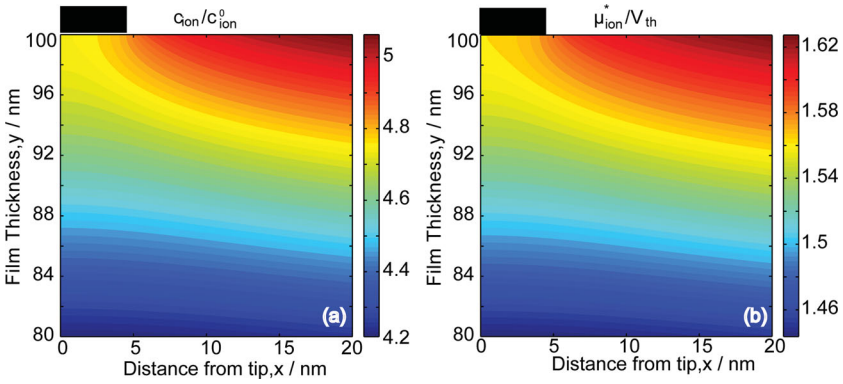

Figure 8. The normalized a) ionic and b) ionic electrochemical potentials for $z_{ion} = 2$ and with $V_0 = -500$ mV. Both distributions are roughly linear in the cross plane. The height of LSCO is 100 nm, the interface LSCO|GDC is at $y = 0$, the tip is at -5 nm<x<5 nm and $y = 100$ nm. Half the thin film is shown. Due to the presence of the tip, the concentration is slightly lower under the tip due to blocking of the reactions.

AFM tip is considered to be purely blocking with respect to ions (non-ionically conductive), and the gas-solid reactions (ORR/OER) occur solely at the Gas|LSCO interface. The reaction rate of oxygen exchange reactions[57–63] can be written as follows:

$$\dot{r} = k_0(p_{O_2}, T)\left(1 - \exp\left(-\frac{\Lambda}{\lambda k_B T}\right)\right) \quad (6)$$

where Λ is the driving "force" of the reaction[63], defined as the difference between the local electrochemical potential and its equilibrium value, λ is a stoichiometric ratio, and $k_0(p_{O_2}, T)$ is a factor which depends on the details of the chemical reactions occurring at the LSCo/gas interface. It is important to note that, while, the influence of oxygen partial pressure and temperature is not addressed due to the experimental limitations, the driving force Λ is a function of the ionic concentration.

The resultant systems of partial differential equations Equations 3–5 and associated boundary conditions described by Equation 6 are fully nonlinear and model the transport of vacancies within the material. Here, the numerical discretization is implemented using a piecewise linear finite element discretization. The solution of the ensuing nonlinear problem is obtained by the Newton method.[64] The electrochemical potential and the distribution of ions are roughly linear in the cross-plane and weakly nonlinear in the in-plane direction (as can be expected given the almost uniform conductivity of material). As shown in the **Figure 8**, the ionic concentration and the electrochemical potential have a nonlinear behavior only in the vicinity of the tip. It is apparent from the right panel that the contour lines intensify near the tip leading to enhance activity in that region.

This numerical analysis allows the main features of surface reaction process to be explored, as illustrated in **Figure 9**. As an example, the area specific surface resistance readily measurable by impedance spectroscopy decays exponentially with the applied bias as shown in Figure 9a, reflecting the balance between the exponentially bias-dependent surface reaction term and the linear ionic concentration drop in the film. The total injected charge scales linearly with the applied voltage in semi-logarithmic scale, see Figure 9b. It is worthwhile noting that at low applied potential the I–V curves, parameterized with respect to the injection coefficient, are parallel in the semi logarithmic scale. When the injection coefficient increases and the applied external potential is large, the nonlinearity in the plot appear. At the same time, mechanical surface displacement (i.e., ESM signal) which is proportional to the average concentration inside the sample $\bar{c}_{ion}$, as a function of the bias has a nonlinear form even in the logarithmic or semilogarithmic scale, indicating as expected an increase of stored ions with increasing bias in the system. Another interesting feature is the injected current profile normalized with respect to its base value, Figure 9d; in this case we consider the injection rate at various voltages for $k_{EX} = k_0$. The injection profile is almost flat at low driving voltage, indicating that the full sample is excited uniformly under those conditions. At higher driving voltage enhanced activity appear near the tip, but never exceed 5% the average driving value.

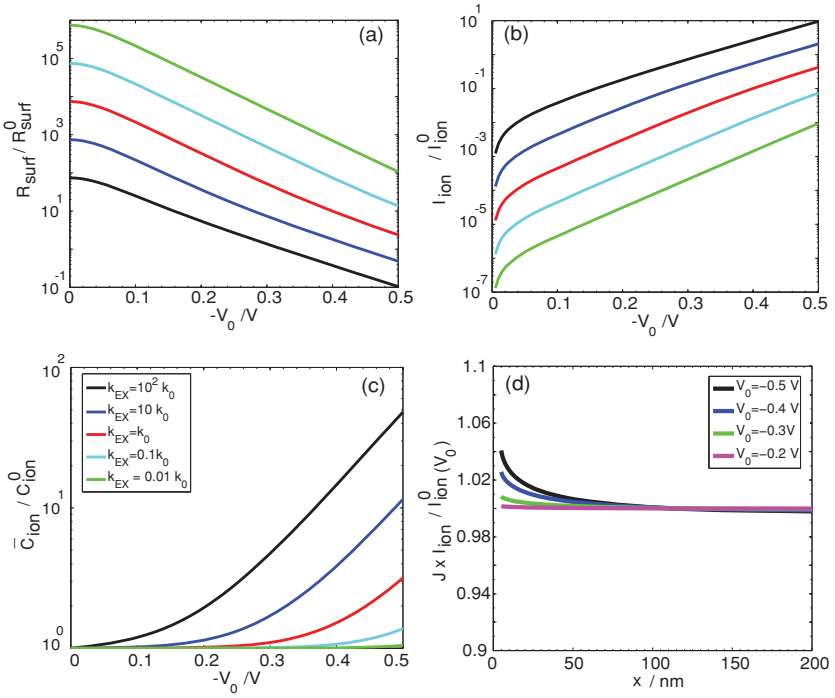

Figure 9. Depiction of the surface reaction a) area specific surface resistance b) total injected current and c) average concentration of ions as a function of the applied bias and the reaction rate coefficient. In panel (d) the injected current profile at the LSCO|gas interface is shown and normalized with respect to the average total current for $k_{EX} = k_0$.

5. Summary

Spatial variability of bias-dependent electrochemical processes on a $(La_{0.5}Sr_{0.5})_2CoO_{4\pm\delta}$-modified $(La_xSr_{1-x})CoO_{3-\delta}$ surface is studied using first-order reversal curve method in electrochemical strain microscopy. The reversible oxygen reduction/evolution process is activated at voltages as low as 3–4 V. First order reversal curve measurements with subsequent cross-correlation analysis allows to differentiate reactivity at the grain and grain boundaries in LSCO. Remarkably, the reaction onset at grains corresponds to lower biases. However, at higher biases, the grain boundaries become preferential reaction sites and dominate overall response. The mechanism of ESM imaging is established and the measured signal is shown to be representative of average surface behavior despite the shadowing effect of the tip. These studies both establish the framework for probing reversible and hysteretic electrochemical processes in solids and illustrate rich spectrum of electrochemical transformations underpinning catalytic activity in cobaltites.

6. Experimental Section

Materials and Methods: The GDC $(Gd_{0.2}Ce_{0.8}O_2)$/LSC113 $(La_{0.8}Sr_{0.2}CoO_{3-\delta})$/LSC214 $(LaSrCoO_{4\pm\delta})$ thin film system was prepared with pulsed laser deposition (PLD) on a YSZ (001) single crystal (9.5 mol% Y_2O_3, Princeton Scientific) with a sintered (1 h, 800 °C) Pt ink (#6082, BASF) counter electrode. The PLD target materials were self-synthesized via the Pecchini method as described previously.[22–24] The following PLD parameters have been utilized: KrF excimer laser, λ = 248 nm, 10 Hz pulse rate, ≈50 mJ pulse energy, $p(O_2)_{PLD\ and\ cooling}$ = 10 mTorr, number of laser pulses: 500 laser pulses of GDC, 15 000 pulses of LSC_{113} and 150 laser pulses of LSC_{214} growth temperatures: T_{GDC} = 450 °C, $T_{LSC113,LSC214}$ = 675 °C. The microelectrodes (/caps) with diameters between ≈200 µm–≈25 µm were prepared using photolithography and acid etching as described previously.[22–24]

ESM Mapping and Spectroscopy: Atomic force microscopy (AFM) and ESM measurements were performed with a commercial system (Asylum Research Cypher) additionally equipped with LabView/MatLab based band excitation controller implemented on a NI-5122/5412 fast AWG and DAQ cards. ESM imaging and spectroscopy was performed with 200–400 kHz 2 V_{pp} band excitation signal applied to a metal coated tip. The spectroscopic measurements were performed at ≈1s/pixel waveform with 2 ms at each dc voltage step. Mapping of the electromechanical response was done typically on a 40 × 40 points grid with a spacing of 20 nm, albeit other spacing and image sizes were also used. All measurements were performed with the biased tip in direct contact with the $LSC_{214//113}$ surface in ambient air and without any additional protective coating.

Modelling of ORR/OER Process: Specifically, we chose that the oxygen partial pressure is given by p_{O_2} = 0.21atm and we estimated[56,65] that $\delta = 10^{-4}$. From Sogaard et al.[66] we estimate that the volume of the elementary cell is $V = 3.989 \times 10^{-28}$ m^3, in turn giving that the ionic concentration at equilibrium is given by $c^0_{ion} = \delta/V = 2.51 \times 10^{-25}$ m^{-3}. The maximum vacancy concentration is $c_{MAX} = 3/V$ giving $p_{MAX} = 3/\delta$. The rigid band model's parameter is temperature independent $g(\varepsilon_F) = 1.91/eV$.[64] Since T = 303.15 K, the thermal voltage is given by $V_{th} = k_B T/e$ = 26.1 mV. We note that the chemical diffusivity is $D_{ion} = 1.45 \times 10^{-27}$ m^2/s,[65] and $\sigma^0_{ion} = 9 \times 10^{-21}$ S/m. The surface reaction rate[67] can be estimated as $K_{EX} = 3.83 \times 10^{-22}$ cm/s, yielding $k = 6.2 \times 10^{-17}$ Cs^{-1} m^{-2}. The dimensions are given by tip radius D_{tip} = 10 nm width of the patterned electrode W = 10 µm and height of the patterned electrode H = 100 nm.

Supporting Information

Supporting Information is available from the Wiley Online Library or from the author.

Acknowledgements

The work was supported by the Materials Science and Engineering Division of the U.S. DOE. This research was conducted in part (A.K., S.V.K., M.B.) at the Center for Nanophase Materials Sciences, which is sponsored at Oak Ridge National Laboratory by the Scientific User Facilities Division, U.S. Department of Energy. MIT group (Y.S.H., E.C., E.M.) acknowledges US DOE (SISGR DESC0002633). E.M. is grateful for financial support from the German Research Foundation (DFG research scholarship). F.C. thanks HKUST for providing start-up funds.

Received: August 22, 2012
Revised: March 13, 2013
Published online: April 17, 2013

[1] V. S. Bagotsky, *Fuel Cells: Problems and Solutions*, Wiley, New York, NY, USA **2009**.
[2] R. O'Hayre, S. W. Cha, W. Colella, F. B. Prinz, *Fuel Cell Fundamentals*, Wiley, New York, NY, USA **2009**.
[3] *High-temperature Solid Oxide Fuel Cells: Fundamentals, Design and Applications* (Eds. S. C. Singhal, K. Kendall), Elsevier, Amsterdam **2003**.
[4] *Apple Hydrogen Fuel Cell Battery Plans Revealed*, http://www.huffingtonpost.com/2011/12/25/apple-hydrogen-battery-phone-computer-plan_n_1169336.html (accessed December 2011).
[5] A. Evans, A. Bieberle-Hutter, J. L. M. Rupp, L. J. Gauckler, *J. Power Sources* **2009**, *194*, 119.
[6] G. J. la O', S. J. Ahn, E. Crumlin, Y. Orikasa, M. D. Biegalski, H. M. Christen, Y. Shao-Horn, *Angew. Chem. Int. Ed.* **2010**, *49*, 5344.
[7] M. Tsuchiya, B. K. Lai, S. Ramanathan, *Nat. Nanotechnol.* **2011**, *6*, 282.
[8] D. J. L. Brett, A. Atkinson, N. P. Brandon, S. J. Skinner, *Chem. Soc. Rev.* **2008**, *37*, 1568.
[9] A. J. Jacobson, *Chem. Mater.* **2010**, *22*, 660.
[10] C. W. Sun, R. Hui, J. Roller, *J. Solid State Electrochem.* **2010**, *14*, 1125.
[11] E. V. Tsipis, V. V. Kharton, *J. Solid State Electrochem.* **2008**, *12*, 1367.
[12] J. Suntivich, H. A. Gasteiger, N. Yabuuchi, H. Nakanishi, J. B. Goodenough, Y. Shao-Horn, *Nat. Chem.* **2011**, *3*, 647.
[13] J. Suntivich, K. J. May, H. A. Gasteiger, J. B. Goodenough, S. H. Yang, *Science* **2011**, *334*, 1383.
[14] J. R. Wilson, W. Kobsiriphat, R. Mendoza, H. Y. Chen, J. M. Hiller, D. J. Miller, K. Thornton, P. W. Voorhees, S. B. Adler, S. A. Barnett, *Nat. Mater.* **2006**, *5*, 541.
[15] M. Kubicek, A. Limbeck, T. Fromling, H. Hutter, J. Fleig, *J. Electrochem. Soc.* **2011**, *158*, B727.
[16] E. J. Crumlin, E. Mutoro, S. J. Ahn, G. J. la O', D. N. Leonard, A. Borisevich, M. D. Biegalski, H. M. Christen, Y. Shao-Horn, *J. Phys. Chem. Lett.* **2010**, *1*, 3149.
[17] J. Januschewsky, M. Ahrens, A. Opitz, F. Kubel, J. Fleig, *Adv. Funct. Mater.* **2009**, *19*, 3151.
[18] F. S. Baumann, J. Fleig, G. Cristiani, B. Stuhlhofer, H. U. Habermeier, J. Maier, *J. Electrochem. Soc.* **2007**, *154*, B931.
[19] S. B. Adler, *Chem. Rev.* **2004**, *104*, 4791.
[20] A. Kumar, F. Ciucci, A. N. Morozovska, S. V. Kalinin, S. Jesse, *Nat. Chem.* **2011**, *3*, 707.

[21] D. Leonard, A. Kumar, S. Jesse, M. Biegalski, H. Christen, E. Mutoro, E. Crumlin, Y. Shao-Horn, S. V. Kalinin, A. Borisevich, *Adv. Energy Mater.* **2013**, DOI: 10.1002/aenm.201200681.
[22] E. Mutoro, E. J. Crumlin, M. D. Biegalski, H. M. Christen, Y. Shao-Horn, *Energy Environ. Sci.* **2011**, *4*, 3689.
[23] N. Balke, S. Jesse, Y. Kim, L. Adamczyk, A. Tselev, I. N. Ivanov, N. J. Dudney, S. V. Kalinin, *Nano Lett.* **2010**, *10*, 3420.
[24] N. Balke, S. Jesse, A. N. Morozovska, E. Eliseev, D. W. Chung, Y. Kim, L. Adamczyk, R. E. Garcia, N. Dudney, S. V. Kalinin, *Nat. Nanotechnol.* **2010**, *5*, 749.
[25] A. N. Morozovska, E. A. Eliseev, N. Balke, S. V. Kalinin, *J. Appl. Phys.* **2010**, *108*, 053712.
[26] A. N. Morozovska, E. A. Eliseev, S. V. Kalinin, *Appl. Phys. Lett.* **2010**, *96*, 222906.
[27] A. N. Morozovska, E. A. Eliseev, S. L. Bravina, F. Ciucci, G. S. Svechnikov, L.-Q. Chen, S. V. Kalinin, *J. Appl. Phys.* **2012**, *111*, 014107.
[28] A. N. Morozovska, E. A. Eliseev, S. V. Kalinin, *J. Appl. Phys.* **2012**, *111*, 011114.
[29] A. N. Morozovska, E. A. Eliseev, G. S. Svechnikov, S. V. Kalinin, *Phys. Rev. B* **2011**, *84*, 045402.
[30] A. N. Morozovska, E. A. Eliseev, S. L. Bravina, S. V. Kalinin, *Phys. Rev. B* **2007**, *75*, 174109.
[31] S. V. Kalinin, B. J. Rodriguez, S. H. Kim, S. K. Hong, A. Gruverman, E. A. Eliseev, *Appl. Phys. Lett.* **2008**, *92*, 152906.
[32] S. V. Kalinin, S. Jesse, B. J. Rodriguez, J. Shin, A. P. Baddorf, H. N. Lee, A. Borisevich, S. J. Pennycook, *Nanotechnology* **2006**, *17*, 3400.
[33] S. Jesse, S. Guo, A. Kumar, B. J. Rodriguez, R. Proksch, S. V. Kalinin, *Nanotechnology* **2010**, *21*, 405703.
[34] S. Jesse, S. V. Kalinin, *J. Phys. D Appl. Phys.* **2011**, *44*, 464006.
[35] S. Jesse, S. V. Kalinin, R. Proksch, A. P. Baddorf, B. J. Rodriguez, *Nanotechnology* **2007**, *18*, 435503.
[36] S. Guo, O. S. Ovchinnikov, M. E. Curtis, M. B. Johnson, S. Jesse, S. V. Kalinin, *J. Appl. Phys.* **2010**, *108*, 084103.
[37] S. Jesse, P. Maksymovych, S. V. Kalinin, *Appl. Phys. Lett.* **2008**, *93*, 112903.
[38] S. Guo, S. Jesse, S. Kalnaus, N. Balke, C. Daniel, S. V. Kalinin, *J. Electrochem. Soc.* **2011**, *158*, A982.
[39] N. Balke, S. Jesse, Y. Kim, L. Adamczyk, I. N. Ivanov, N. J. Dudney, S. V. Kalinin, *ACS Nano* **2010**, *4*, 7349.
[40] S. Jesse, H. N. Lee, S. V. Kalinin, *Rev. Sci. Instrum.* **2006**, *77*, 073702.
[41] S. V. Kalinin, A. N. Morozovska, L. Q. Chen, B. J. Rodriguez, *Rep. Prog. Phys.* **2010**, *73*, 056502.
[42] I. D. Mayergoyz, *Mathematical Models of Hysteresis and Their Applications*, Elsevier, New York, NY, USA **2003**.
[43] J. Fleig, *Solid State Ionics* **2003**, *161*, 279.
[44] A. Sawa, *Mater. Today* **2008**, *11*, 28.
[45] D. B. Strukov, G. S. Snider, D. R. Stewart, R. S. Williams, *Nature* **2008**, *453*, 80.
[46] T. Tsuruoka, K. Terabe, T. Hasegawa, M. Aono, *Nanotechnology* **2010**, *21*, 425205.
[47] R. Waser, M. Aono, *Nat. Mater.* **2007**, *6*, 833.
[48] R. Waser, R. Dittmann, G. Staikov, K. Szot, *Adv. Mater.* **2009**, *21*, 2632.
[49] J. J. Yang, F. Miao, M. D. Pickett, D. A. A. Ohlberg, D. R. Stewart, C. N. Lau, R. S. Williams, *Nanotechnology* **2009**, *20*, 215201.
[50] W. Jiang, M. Noman, Y. M. Lu, J. A. Bain, P. A. Salvador, M. Skowronski, *J. Appl. Phys.* **2011**, *110*, 054514.
[51] D. Lee, A. Yoon, S. Y. Jang, J. G. Yoon, J. S. Chung, M. Kim, J. F. Scott, T. W. Noh, *Phys. Rev. Lett.* **2011**, *107*, 057602.
[52] H. T. Yi, T. Choi, S. G. Choi, Y. S. Oh, S. W. Cheong, *Adv. Mater.* **2011**, *23*, 3403.
[53] F. Ciucci, Y. Hao, D. G. Goodwin, *Phys. Chem. Chem. Phys.* **2009**, *11*, 11243.
[54] M. H. R. Lankhorst, H. J. M. Bouwmeester, *J. Electrochem. Soc.* **1997**, *144*, 1261.
[55] M. H. R. Lankhorst, H. J. M. Bouwmeester, H. Verweij, *J. Solid State Chem.* **1997**, *133*, 555.
[56] M. H. R. Lankhorst, H. J. M. Bouwmeester, H. Verweij, *Solid State Ionics* **1997**, *96*, 21.
[57] J. Maier, *Solid State Ionics* **1998**, *112*, 197.
[58] J. Fleig, J. Jamnik, *J. Electrochem. Soc.* **2005**, *152*, E138.
[59] W. Lai, S. M. Haile, *J. Am. Ceramic Soc.* **2005**, *88*, 2979.
[60] J. Fleig, *Phys. Chem. Chem. Phys.* **2005**, *7*, 2027.
[61] J. Fleig, R. Merkle, J. Maier, *Phys. Chem. Chem. Phys.* **2007**, *9*, 2713.
[62] D. S. Mebane, M. Liu, *J. Solid State Electrochem.* **2007**,*10*, 575.
[63] S. B. Adler, X. Y. Chen, J. R. Wilson, *J. Catal.* **2007**, *245*, 91.
[64] S. C. Brenner, L. G. Scott, *The Mathematical Theory of Finite Element Methods*, Vol. *15*, Springer - Verlag, New York, NY, USA **2000**.
[65] A. J. Bard, L. R. Faulkner, *Electrochemical Methods: Fundamentals and Applications*, Wiley John & Sons, 2nd ed., New York, USA **2000**.
[66] M. Sogaard, P. V. Hendriksen, M. Mogensen, F. W. Poulsen, E. Skou, *Solid State Ionics* **2006**, *177*, 3285.
[67] A. V. Berenov, A. Atkinson, J. A. Kilner, E. Bucher, W. Sitte, *Solid State Ionics* **2010**, *181*, 819.